ACS APPLIED MATERIALS & INTERFACES

Research Article

www.acsami.org

Structure and Composition of $Zn_xCd_{1-x}S$ Films Synthesized through Chemical Bath Deposition

B. Selin Tosun,[†] Chelsea Pettit,[†] Stephen A. Campbell,[‡] and Eray S. Aydil*[,†]

[†]Department of Chemical Engineering and Materials Science, University of Minnesota, 421 Washington Avenue SE, Minneapolis, Minnesota 55455, United States

[‡]Department of Electrical and Computer Engineering, University of Minnesota, 200 Union Street, Minneapolis, Minnesota 55455, United States

ABSTRACT: Zinc cadmium sulfide ($Zn_xCd_{1-x}S$) thin films grown through chemical bath deposition are used in chalcopyrite solar cells as the buffer layer between the n-type zinc oxide and the p-type light absorbing chalcopyrite film. To optimize energetic band alignment and optical absorption, advanced solar cell architectures require the ability to manipulate x as a function of distance from the absorber−ZnCdS interface. Herein, we investigate the fundamental factors that govern the evolution of the composition as a function of depth in the film. By changing the initial concentrations of Zn and Cd salts in the bath, the entire range of overall compositions ranging from primarily cubic ZnS to primarily hexagonal CdS could be deposited. However, films are inhomogeneous and x varies significantly as function of distance from the film−substrate interface. Films with high overall Zn concentration ($x > 0.5$) exhibit a Cd-rich layer near the film−substrate interface because Cd is more reactive than Zn. This layer is typically beneath a nearly pure ZnS film that forms after the Cd-rich layers are deposited and Cd is depleted in the bath. In films with high overall Cd concentration ($x < 0.5$) the Zn concentration rises towards the film's surface. Fortunately, these gradients are favorable for solar cells based on low band gap chalcopyrite films.

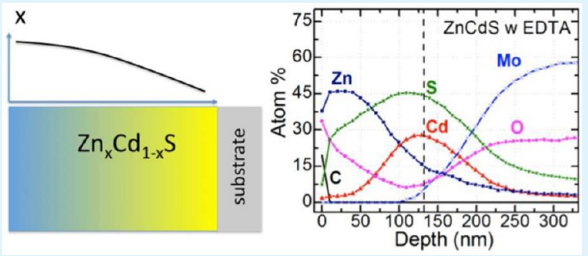

KEYWORDS: *cadmium sulfide, copper indium gallium diselenide, photovoltaics, solar cell, zinc sulfide*

INTRODUCTION

Amongst the second generation thin film solar cells, those based on the copper indium gallium diselenide ($CuIn_{1-x}Ga_xSe_2$ or CIGS) absorber have the distinction of having the highest overall power conversion efficiencies (20.3%).[1−6] The p−n junction in the CIGS solar cell is between a p-type CIGS absorber and a 50−100 nm thick n-type cadmium sulfide (CdS) layer grown on the CIGS through chemical bath deposition (CBD).[6−15] A nominally intrinsic oxide (e.g., ZnO) is deposited on the CdS film to complete the p−n junction and, for this reason, the CdS is often referred to as the buffer layer. The CBD−CdS buffer layer is crucial for achieving high efficiencies. CdS films have also been synthesized through other methods including molecular beam epitaxy,[16] metal−organic vapor phase epitaxy,[17] spray pyrolysis,[18] magnetron sputtering,[19] photochemical,[20] sol−gel,[21] and atomic layer deposition.[22] The main role of the CdS is to keep the Fermi level at the interface above the middle of the CIGS band gap. In addition, CdS is lattice-matched to CIGS and protects the p−n junction from physical damage during sputtering of ZnO.[14] Even though physical or chemical vapor deposition methods would be more convenient than CBD, solar cells made with CdS films deposited through these vacuum-based approaches have not been able to match the high efficiencies obtained using CBD−CdS. There appears to be a process in CBD that modifies the CIGS−CdS interface but this process is not easily duplicated in vacuum deposition. It has been suggested that the CBD process dopes the surface of the CIGS layer n-type and results in a buried homojunction within the absorber's subsurface region.[23] CBD−CdS films are also used in the emerging copper zinc tin sulfide (or selenide) based solar cells.[24,25]

There has always been an interest in replacing CdS with $Zn_xCd_{1-x}S$ ($0 \le x < 1$) both to reduce or to eliminate Cd and to be able to widen the band gap of this layer.[26−39] The narrow bandgap CdS ($E_g \approx 2.41$ eV) partially blocks the transmission of high-energy photons to the absorber layer below and decreases the power conversion efficiency. While thinner CdS layers maybe used to mitigate this blocking, very thin CdS layers result in low shunt resistance in the solar cells, and reduce the fill factor.[40,41] When CdS is replaced with ZnS, the wider band gap of ZnS (3.7 eV) leads to higher quantum efficiency in the blue region of the electromagnetic spectrum,[42] but despite this increase, the overall power conversion efficiency decreases from over 20% to 19%.[43] The decrease in the power conversion efficiency is attributed to the increase in the conduction band offset between CIGS and the ZnS buffer layer which results in lower short circuit current density (J_{sc})

Received: May 2, 2012
Accepted: June 25, 2012
Published: June 25, 2012

and lower fill factor.[44] Solar cells with buffer layers comprised of ZnS deposited on a very thin CdS were more efficient than solar cells with just CdS or just ZnS films.[44] The improved performance with this dual buffer layer architecture is attributed to the better band alignment at the CdS/CIGS interface and higher transmission through the ZnS.[44] An alternative and particularly elegant way to obtain higher transmission and improved performance is by using size quantized CdS.[45]

Multijunction CIGS-based solar cells require wider band gap absorber layers than CIGS such as copper indium aluminum gallium diselenide ($CuIn_{1-x-y}Al_yGa_xSe_2$ or CIAGS). In solar cells made with CIAGS films, the conduction band offset between the absorber and CdS layer will be larger, leading to increased recombination rates at the junction and lower solar cell efficiencies.[44,46] Depending on the band gap of the absorber layer (e.g., Al and Ga concentrations in the film), it is desired to adjust the band gap of the $Zn_xCd_{1-x}S$ buffer layer by adjusting x to reduce "cliff" and "spike" type discontinuities.[47] The ability to manipulate x as a function of distance from the absorber-$Zn_xCd_{1-x}S$ interface may also be desired to simultaneously optimize the energetic band alignment, the optical absorption and the internal electric field in the junction.

While $Zn_xCd_{1-x}S$ films have been deposited by CBD,[27,39,49] the structure and composition of these films have not been studied in detail. It is often assumed that the film composition (e.g., x) is homogenous in the direction normal to the substrate surface. Herein, we deposit and characterize $Zn_xCd_{1-x}S$ films with $0 \leq x \leq 1$ and show that the chemistry of the CBD method leads to a variety of film structures and composition variations within the film. These variations are brought about by the differences in the Cd and Zn ion reaction rates and equilibria.

$Zn_xCd_{1-x}S$ films are typically deposited from aqueous solutions containing thiourea, $ZnSO_4$, $CdSO_4$ and ammonia.[43] Ammonia complexes with the metal ions, increases the pH (~10.5) and decomposes the thiourea to release sulfur ions into solution.[49] The chemical reactions taking place in $Zn_xCd_{1-x}S$ CBD are listed in Table 1.[42]

Metal sulfide CBD is understood in terms of two competing reaction mechanisms,[50,51] the ion-by-ion and cluster-by-cluster deposition mechanisms. The dominant mechanism is determined by many factors including the ratio of the free metal ions to complexing agent, pH and concentrations of the metal ions. In the ion-by-ion deposition, the metal and the sulfur ions react heterogeneously to form the metal−sulfide, CdS or ZnS. This mechanism is operative when the free Cd^{2+} and Zn^{2+} concentrations are low and, consequently, the deposition is slow.[49−53] In addition, the ion-by-ion deposition leads to larger crystals in the deposited films.[52] In cluster-by-cluster mechanism, the S^{2-} ions are thought to react with very small colloidal particles or clusters of metal-hydroxide either on the surface of the growing film or in the solution. This mechanism is thought to become increasingly more important as the concentrations of the metal ions are increased.[49] Since the solubility product of CdS is smaller than that for ZnS (e.g., reaction 11 in Table 1), and $Cd(OH)_2$ reacts faster with S^{2-} than $Zn(OH)_2$, CdS growth is dominated by the ion-by-ion deposition mechanism, while ZnS growth is dominated by the cluster-by-cluster deposition mechanism. However, the deposition mechanism can be shifted from cluster-by-cluster to ion-by-ion mechanism by reducing the Zn^{2+} and Cd^{2+} ion concentration in the solution. This can be achieved by using strong chelating agents, such as ethylenediaminetetraacetic acid disodium (EDTA) or sodium citrate, which slow the release of Zn^{2+} and Cd^{2+} ions to the solution[43] [reactions 12 and 13 in Table 1]. This strategy also results in lower hydroxide incorporation into the growing films.[53]

Table 1. Important Reactions in $Zn_xCd_{1-x}S$ CBD[a]

$$SC(NH_2)_{2(s)} + OH^-_{(aq)} \leftrightarrow SH^-_{(aq)} + CH_2N_{2(aq)} + H_2O_{(aq)} \quad (1)$$

$$NH_4{}^+_{(aq)} + OH^-_{(aq)} \leftrightarrow NH_{3(aq)} + H_2O \quad (2)$$

$$ZnSO_{4(s)} \leftrightarrow Zn^{2+}_{(aq)} + SO_4{}^{2-}_{(aq)} \quad (3)$$

$$CdSO_{4(s)} \leftrightarrow Cd^{2+}_{(aq)} + SO_4{}^{2-}_{(aq)} \quad (4)$$

$$Zn^{2+}_{(aq)} + 4NH_{3(aq)} \leftrightarrow [Zn(NH_3)_4]^{2+}_{(aq)} \; K = 10^{8.9} \quad (5)$$

$$Cd^{2+}_{(aq)} + 4NH_{3(aq)} \leftrightarrow [Cd(NH_3)_4]^{2+}_{(aq)} \; K = 10^{6.9} \quad (6)$$

$$SH^-_{(aq)} + OH^-_{(aq)} \leftrightarrow S^{2-}_{(aq)} + H_2O \quad (7)$$

$$Zn^{2+}_{(aq)} + 2OH^-_{(aq)} \leftrightarrow Zn(OH)_{2(s)} \; K_s = 10^{-16} \quad (8)$$

$$Cd^{2+}_{(aq)} + 2OH^-_{(aq)} \leftrightarrow Cd(OH)_{2(s)} \; K_s = 10^{-13.7} \quad (9)$$

$$Zn^{2+}_{(aq)} + S^{2-}_{(aq)} \leftrightarrow ZnS_{(s)} \; K_{sp} = 10^{-24.7} \quad (10)$$

$$Cd^{2+}_{(aq)} + S^{2-}_{(aq)} \leftrightarrow CdS_{(s)} \; K_{sp} = 10^{-27} \quad (11)$$

$$Zn^{2+}_{(aq)} + EDTA^{2-}_{(aq)} \leftrightarrow Zn(EDTA)^{2+}_{(aq)} \; K = 10^{16.5} \quad (12)$$

$$Cd^{2+}_{(aq)} + EDTA^{2-}_{(aq)} \leftrightarrow Cd(EDTA)^{2+}_{(aq)} \; K = 10^{16.46} \quad (13)$$

$$[Zn(NH_3)_{4-x}EDTA_x]^{2(x-1)-}_{(aq)} + SC(NH_2)_{2(aq)} + 2OH^-_{(aq)} \rightarrow [ZnS]_{(s)} + EDTA_{(aq)} + NH_{3(aq)} + CN_2H_{2(aq)} + H_2O \quad (14)$$

$$[Cd(NH_3)_{4-x}EDTA_x]^{2(x-1)-}_{(aq)} + SC(NH_2)_{2(aq)} + 2OH^-_{(aq)} \rightarrow [CdS]_{(s)} + EDTA_{(aq)} + NH_{3(aq)} + CN_2H_{2(aq)} + H_2O \quad (15)$$

[a]Reactions 12−15 are important in presence of a chelating agent, such as EDTA.

EXPERIMENTAL SECTION

The $Zn_xCd_{1-x}S$ films were deposited on 1 inch × 1 inch pieces of bare or Mo-coated Si (100) wafers. The 750 nm thick Mo film was deposited using sputtering. The substrates were cleaned ultrasonically in a de-ionized (DI) water, acetone and isopropanol mixture (1:1:1 ratio by volume) and dried by blowing compressed air across the substrate. A piece of kapton tape was used to cover a small section of the substrate to create a step for measuring the film thickness using a profilometer (KLA-Tencor P-16 Surface Profiler). During deposition, the CBD solution was stirred continuously using a 9.5 mm magnetic stirring bar at 400 rpm. The CBD solutions were prepared at room temperature by adding the following chemicals to DI water in order, cadmium sulfate ($CdSO_4$), ammonium hydroxide (NH_4OH), EDTA, zinc sulfate ($ZnSO_4$), and thiourea ($SC(NH_2)_2$). The total solution volume was 120 mL. In all depositions, the ammonium hydroxide concentration in the solution was kept constant at 3 M. The concentration of other reactants was changed to study their effects on the deposition rate and film properties. Typically, the $ZnSO_4$ concentration was kept higher than $CdSO_4$ concentration because of the lower reaction rate of Zn. A 250 mL salted bath water was heated prior to start of the deposition to 103−105 °C and the beaker containing the CBD solution was placed in this bath at $t = 0$ s. In the mean time, the substrates were placed in the solution beaker. The beaker with the CBD solution and the substrates was placed in the heating bath after the bath reached 103 °C. The reaction solution started to become turbid within 8−15 minutes as both the solution and bath temperatures reach ~85 °C simultaneously. The substrates were kept in the heated CBD solution for 1−3 h. The substrates were

removed from the chemical bath after 1, 2, and 3 h, rinsed with DI-water, ultrasonically cleaned and then dried using compressed air.

The film thicknesses were measured with a profilometer and confirmed with single wavelength and spectroscopic ellipsometry as well as scanning electron microscopy (SEM, Jeol 6500). Energy-dispersive X-ray spectroscopy (EDS, Thermo-Noran Vantage SIX) was used for the elemental analysis of the deposited films. The accelerating voltage was kept constant as 7.5 keV. The spatially averaged (across thickness and across lateral dimensions) elemental concentrations were determined using the $\pi-\rho-z$ method with theoretical standard element sensitivity factors after subtracting the background from the acquired X-ray spectra. Mo L_α emission (2.290 keV) is very close to S K_α emission (2.306 keV) and they overlap in EDS. Hence the S concentration in the films deposited on Mo can not be detected accurately. The structural properties of the films were studied using X-ray diffraction (XRD, Bruker-AXS) with Cu–K_α radiation (λ = 0.154056 nm). The variation of the film's composition as a function of position perpendicular to the substrate surface was studied using depth profiling by Auger electron spectroscopy (AES, Physical Electronics Model 545), and film thicknesses (and, thus, Auger sputtering rates) were calibrated using spectroscopic ellipsometry measurements. Argon ions were used for sputtering during Auger depth profiling and the sputtering rate varied between 5.6 nm/min for CdS to 10.7 nm/min for ZnS.

If the EDTA concentration is too high for a given $CdSO_4$ or $ZnSO_4$ concentration, the chelation equilibrium leads to very low Cd^{2+} and Zn^{2+} concentrations and no film is deposited. The appropriate EDTA concentrations were found by depositing CdS and ZnS using different $CdSO_4$-to-EDTA and $ZnSO_4$-to-EDTA ratios, respectively. Figure 1a and 1b shows the regions of the $CdSO_4$-EDTA and $ZnSO_4$-EDTA planes where CdS and ZnS deposition is possible. Figure 1a and 1b shows that CdS deposition requires a $CdSO_4$-to-EDTA ratio of at least ~0.3 and ZnS deposition requires a $ZnSO_4$-to-EDTA ratio of at least ~2.5. The higher surface roughness in Mo-coated Si (100) leads to film nucleation (or smaller incubation time) and deposition at low $ZnSO_4$-to-EDTA ratios which does not result in films on bare Si (100) substrates. In the no-deposition regions of Figure 1a and 1b, the Si substrate is etched and Mo peels off the silicon. The EDTA concentrations in our experiments were guided by Figure 1a and 1b. When depositing $Zn_xCd_{1-x}S$ films, we kept the overall EDTA concentration constant at 20 mM while changing the $ZnSO_4$ and $CdSO_4$ concentrations to achieve different x. $ZnSO_4$ and $CdSO_4$ concentrations were chosen to remain above the lines in Figures 1a and 1b.

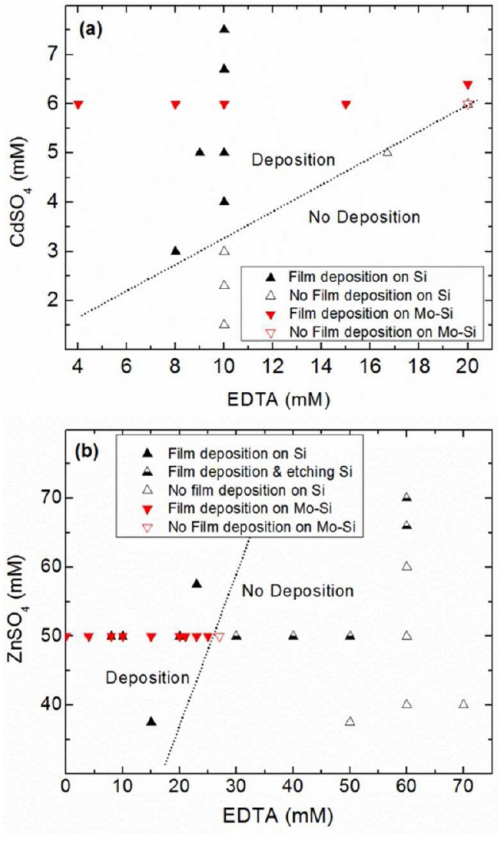

Figure 1. Region of the (a) $CdSO_4$–EDTA and (b) $ZnSO_4$–EDTA parameter space where (a) CdS and (b) ZnS films are obtained. The ammonium hydroxide and thiourea concentrations were kept constant at 3 M and 0.6 M, respectively.

RESULTS AND DISCUSSION

Film Structure. Figure 2 shows the XRD patterns from films deposited with various initial $CdSO_4$ and $ZnSO_4$ concentrations on Mo-coated Si (100) substrates. The XRD from the Mo (110) diffraction at 2θ = 40.7° is used as a reference. The films deposited only with $ZnSO_4$ exhibit a broad asymmetric diffraction peak at ~29.2° shifted by 0.63° to higher 2θ values from the (111) diffraction peak of cubic ZnS (sphalerite) and from the (002) diffraction of hexagonal ZnS (wurtzite), which diffract at the same 2θ. This shift indicates a lattice strain of about 2.13 %. This contraction may be due to incorporation of O into the film: O was detected in the films by AES (*vide infra*). The asymmetry indicates the presence of some hexagonal ZnS. Indeed Figure 3 shows a deconvolution of the peak at $2\theta \approx 29.2°$ into three contributions representing diffractions from the (100), (002), and (101) planes of hexagonal ZnS and from the (111) planes of cubic ZnS. The (002) diffraction from hexagonal ZnS and the (111) diffraction from cubic ZnS overlap and are represented using a single peak. Formation of cubic zinc blende is not surprising because cubic ZnS is the thermodynamically stable phase at low temperatures.[54] Hexagonal phases can be incorporated into the growing film through the formation of stacking faults during

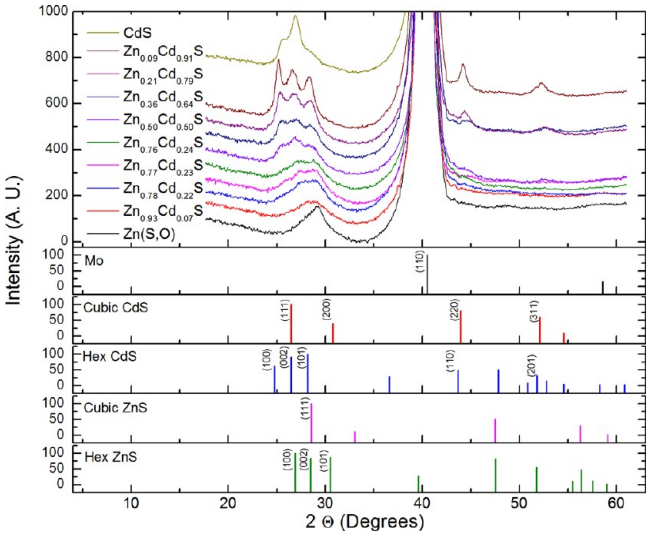

Figure 2. X-ray diffraction from $Zn_xCd_{1-x}(S,O)$ films deposited on Mo-coated Si(100) substrates for 3 h using various initial concentrations of $ZnSO_4$ and $CdSO_4$ in the CBD solution (please see the legend). Ammonium hydroxide, thiourea, and EDTA concentrations were 3, 0.6, and 0.02 M, respectively. XRD expected from various polycrystalline sulfides and Mo are shown below the experimental data.

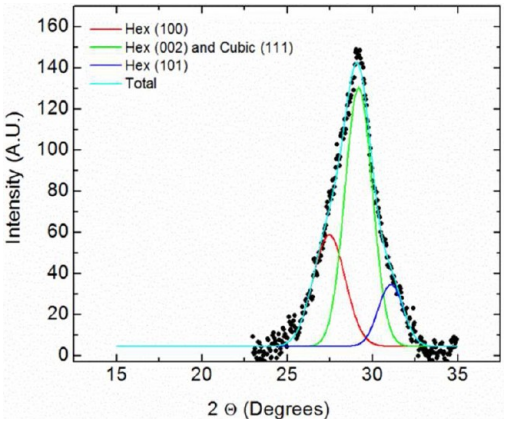

Figure 3. Deconvolution of the XRD peak at 2θ = 29.2 into three contributions representing diffractions from the (100), (002), and (101) planes of hexagonal ZnS and from the (111) planes of cubic ZnS. The (002) and (111) diffractions appear at the same location and were fitted with a single peak.

Table 2. Average Composition and Thickness of $Zn_xCd_{1-x}(S,O)$ Films Deposited on Mo-Coated Si (100) Substrates As a Function of Initial $ZnSO_4$ and $CdSO_4$ Concentrations in the Solution[a]

$[ZnSO_4]$ (mM)	$[CdSO_4]$ (mM)	thickness (nm)	$Zn_xCd_{1-x}(S,O)$
50	0.00	204	Zn(S,O)
49	0.10	186	$Zn_{0.93}Cd_{0.07}(S,O)$
48	0.25	167	$Zn_{0.78}Cd_{0.22}(S,O)$
46	0.50	133	$Zn_{0.77}Cd_{0.23}(S,O)$
42	1.00	104	$Zn_{0.76}Cd_{0.24}(S,O)$
39	1.33	129	$Zn_{0.50}Cd_{0.50}(S,O)$
36	1.67	82	$Zn_{0.36}Cd_{0.64}(S,O)$
33	2.00	115	$Zn_{0.21}Cd_{0.79}(S,O)$
17	4.00	117	$Zn_{0.09}Cd_{0.91}(S,O)$
0	6.00	85	CdS

[a]Compositions correspond to films that were deposited for 3 h. Ammonium hydroxide, thiourea and EDTA concentrations were kept constant at 3 M, 0.6 M and 0.02 M, respectively. The ratio of $[ZnSO_4]$ to $[CdSO_4]$ concentrations is varied such as to lie above the lines in Figure 1a and 1b.

low temperature growth. The addition of $CdSO_4$ to the growth solution incorporates Cd into the film (Table 1) and shifts the ZnS diffraction peak at $2\theta \approx 29.2°$ to lower angles. With enough $CdSO_4$ addition, three diffraction peaks corresponding to a hexagonal structure with lattice parameters close to those of CdS appear. These peaks seem to appear between x = 0.76 and x = 0.5 and grow as x decreases, consistent with the theoretical study by Wright and Gale.[54] For example, the films deposited using 17 mM $ZnSO_4$ and 4 mM $CdSO_4$ (x = 0.09) clearly show the (100), (002), and (101) hexagonal CdS diffractions. The ratios of the (100), (002), and (101) peaks in CdS films deposited using $CdSO_4$ alone do not match the ratios expected from a polycrystalline diffraction pattern. Two-dimensional diffraction patterns show rings indicating that the films are not textured. Thus, we conclude that the CdS films (x = 0) are primarily hexagonal with some cubic CdS incorporated in the film. We note that the XRD probes the entire film and the diffractions patterns for $Zn_xCd_{1-x}S$ films may contain more than one phase. For example, films where the average composition is between x = 0 and x = 1 may be mixtures of

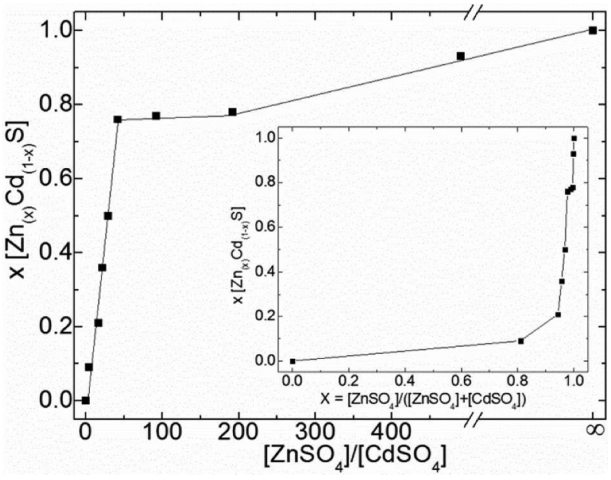

Figure 4. Composition variable x versus the $ZnSO_4$-to-$CdSO_4$ concentration ratio. The inset shows the composition variable versus the initial fraction of $ZnSO_4$ in the chemical bath, x = $[ZnSO_4]$/($[ZnSO_4]$ + $[CdSO_4]$).

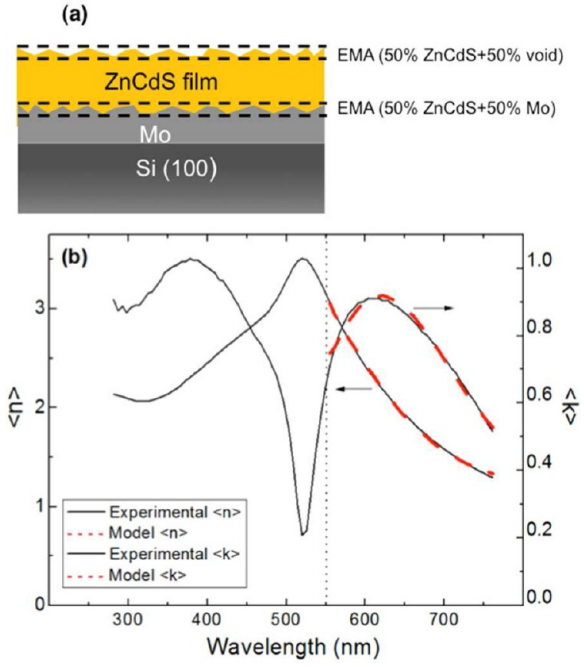

Figure 5. (a) Three-layer optical model of the film used for modeling the spectroscopic ellipsometry data. The film is modeled as consisting of three layers, an interface roughness layer model as a 50%/50% mixture of Mo and the sulfide film, the sulfide film and a surface roughness layer model as a 50%/50% mixture of voids and the sulfide film. The roughness layers are modeled using Bruggeman effective medium approxination. (b) A typical fit of pseudo-n and pseudo-k data for a CdS film.

the cubic $Zn_yCd_{1-y}S$ and hexagonal $Zn_zCd_{1-z}S$ with z and y such that the overall composition is x.

Film Composition. Table 2 shows the $Zn_xCd_{1-x}(S,O)$ film composition as a function of the initial $CdSO_4$ and $ZnSO_4$ concentrations in the CBD solutions. These films were deposited on Mo-coated Si(100) substrates. Zn and Cd stoichiometry was calculated from EDS. The sulfur peak overlaps with that of Mo so that its concentration cannot be determined using EDS. From AES data we know that the films

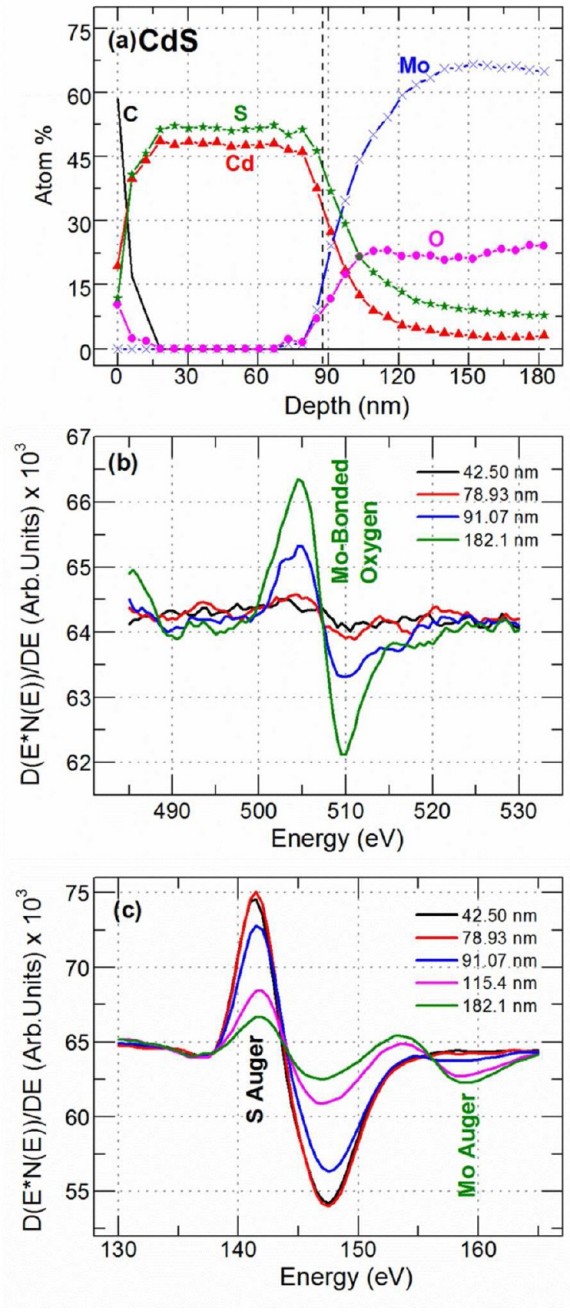

Figure 6. (a) Auger depth profile of an 85 nm thick CdS film deposited on Mo-coated Si(100) substrates, (b) oxygen region of the auger spectrum of this CdS film at different depths, (c) sulfur region of the auger spectrum of this CdS film at different depths.

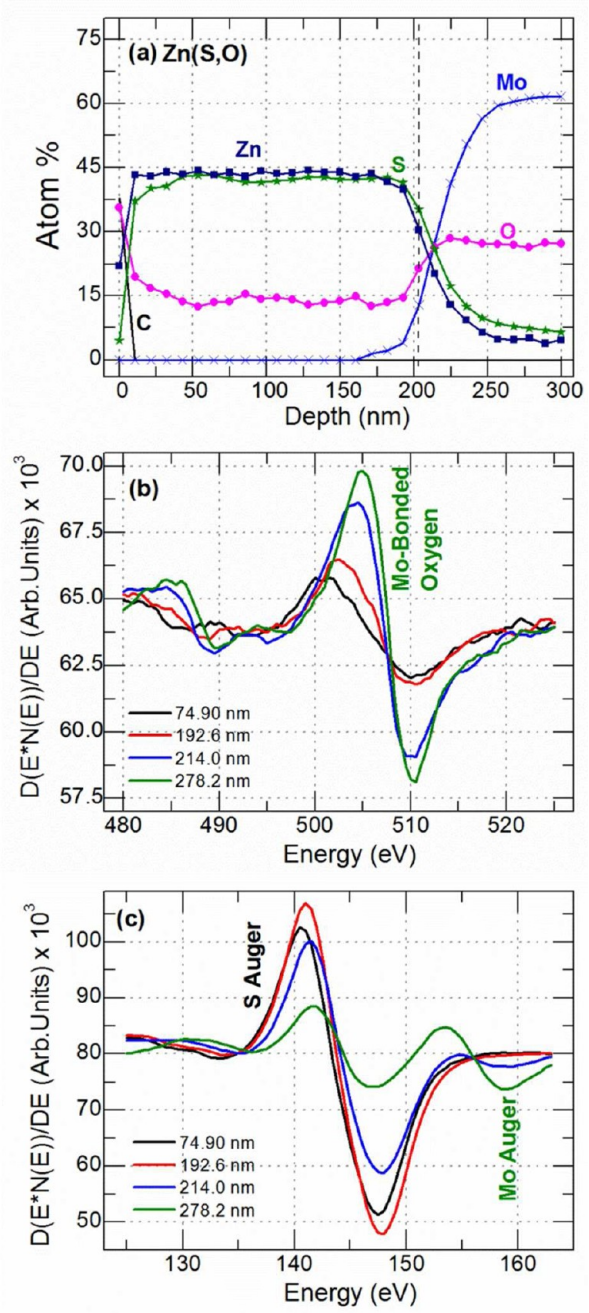

Figure 7. (a) Auger depth profile of an 204 nm thick ZnS film deposited on Mo-coated Si(100) substrates, (b) oxygen region of the auger spectrum of this ZnS film at different depths, and (c) sulfur region of the auger spectrum of this ZnS film at different depths.

contain S and O so that we refer to these films as $Zn_xCd_{1-x}(S,O)$. Clearly, increasing the $ZnSO_4$ concentration in the solution increases the average Zn concentration, x, in the film, though the increase is not linear with the solution composition, Figure 4 shows x versus $[ZnSO_4]/[CdSO_4]$ ratio. The average Zn concentration in the film increases linearly from 0 to ~0.75 with increasing $[ZnSO_4]/[CdSO_4]$ ratio. Increasing it beyond 0.75 requires a steeper increase in the $[ZnSO_4]/[CdSO_4]$ ratio.

Since the bath composition changes with time during the deposition, we expected Zn and Cd concetration gradients within the film. Consequently, we examined the film composition as a function of depth into the film using AES depth profiling. The $Zn_xCd_{1-x}(S,O)$ film thicknesses from spectroscopic ellipsometry in conjunction with the shifts in the AES spectra were used to locate the Mo−$Zn_xCd_{1-x}(S,O)$ film interface. The details of our approach for determining the film composition as a function of depth are as follows.

First, the thicknesses of the $Zn_xCd_{1-x}(S,O)$ films were determined using spectroscopic ellipsometry, which also provided information on the surface and interfacial roughness. The refractive index of the films for wavelengths longer than 550 nm (2.25 eV) could only be fit if the three-layer model shown in Figure 5 was used. The three-layer model consisted of an interfacial roughness layer between Mo and the

dx.doi.org/10.1021/am300771k | ACS Appl. Mater. Interfaces 2012, 4, 3676−3684

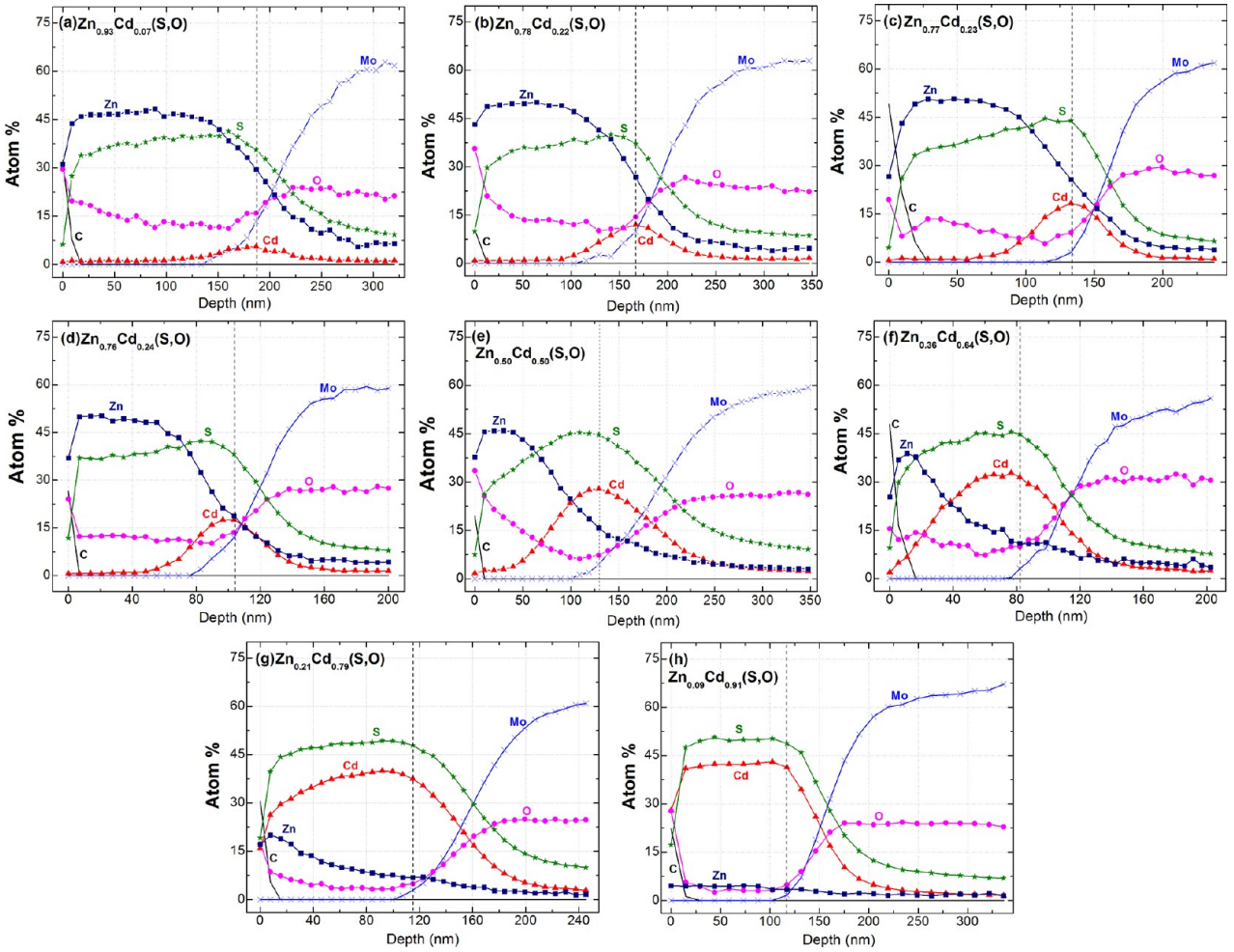

Figure 8. Auger depth profiles for (a) $Zn_{0.93}Cd_{0.07}(S,O)$, (b) $Zn_{0.78}Cd_{0.22}(S,O)$, (c) $Zn_{0.77}Cd_{0.23}(S,O)$, (d) $Zn_{0.76}Cd_{0.24}(S,O)$, (e) $Zn_{0.5}Cd_{0.5}(S,O)$, (f) $Zn_{0.36}Cd_{0.64}(S,O)$, (g) $Zn_{0.21}Cd_{0.79}(S,O)$, and (h) $Zn_{0.09}Cd_{0.91}(S,O)$ films.

$Zn_xCd_{1-x}(S,O)$ film, the $Zn_xCd_{1-x}(S,O)$ film, and a surface roughness layer. This model is shown schematically in Figure 5 along with a typical fit to a CdS film. The Cauchy equation was used for modeling the optical properties of the $Zn_xCd_{1-x}(S,O)$ films only in the region where the film is transparent (λ > 550 nm). Later, we show that the film composition changes throughout the film gradually with respect to the wavelength of light. Nevertheless, Cauchy model could be used to represent the film's refractive index and to determine the film thickness accurately but the Cauchy model parameters varied from film to film. The roughness layers between Mo- and the $Zn_xCd_{1-x}(S,O)$ and on the surface of the $Zn_xCd_{1-x}(S,O)$ film were modeled using the effective medium approximation. The former consisted of 50% Mo and 50% $Zn_xCd_{1-x}(S,O)$ and the latter consisted of 50 % voids and 50 % $Zn_xCd_{1-x}(S,O)$. The thicknesses of the three layers were adjusted to fit the optical data.

Second, the location of the Mo−$Zn_xCd_{1-x}(S,O)$ film interface was determined from the shifts in the AES peaks. The AES of the elements, especially anions, showed characteristic shifts at the Mo−$Zn_xCd_{1-x}(S,O)$ film interface. The spectrum at which the shift occurred was assigned to be the interface and the depth at that point was taken to be the value of the top two layers of the 3-layer optical model film thickness determined using spectroscopic ellipsometry.

For example, Figure 6a shows the elemental Auger depth profile of an 85 nm thick CdS film. Figure 6b and 6c shows selected Auger electron spectra recorded as one approaches and sputters through the Mo-CdS film interface. There are two indications when sputtering reaches the Mo-CdS film interface. First, as the sputtered surface reaches the Mo layer, the oxygen Auger peak increases (Figure 6b). Our Mo films always contain oxygen both due to incorporation during sputtering and due to grain boundary oxidation after the film is taken outside the sputtering chamber. Additional oxidation of the grain boundaries may also be taking place in the basic CBD solution prior to CdS nucleation and growth. This residual oxygen was convenient to locate the interface between the CdS and the Mo films. The shift in the sulfur and the rise in the Mo Auger spectra are two additional indicators of the Mo−$Zn_xCd_{1-x}S$ film interface. Figure 6c shows that there is a very small but detectable shift in the S Auger peak accompanied by the appearance of the Mo Auger peak at ∼153 eV as the Mo-CdS interface is reached. We assign the spectrum at which we begin detecting Mo and O to a depth of 85 nm, the sum of the surface roughness layer (∼ 20 nm) and the bulk CdS film (∼ 65 nm) thicknesses. The Auger depth profile shows a uniform CdS film between ∼15 nm and ∼85 nm. Adventitious C and O are detected at the surface, which decay to the noise level after sputtering approximately 15 nm of the film's surface, about the thickness of the surface roughness layer. Both cadmium and

dx.doi.org/10.1021/am300771k | ACS Appl. Mater. Interfaces 2012, 4, 3676−3684

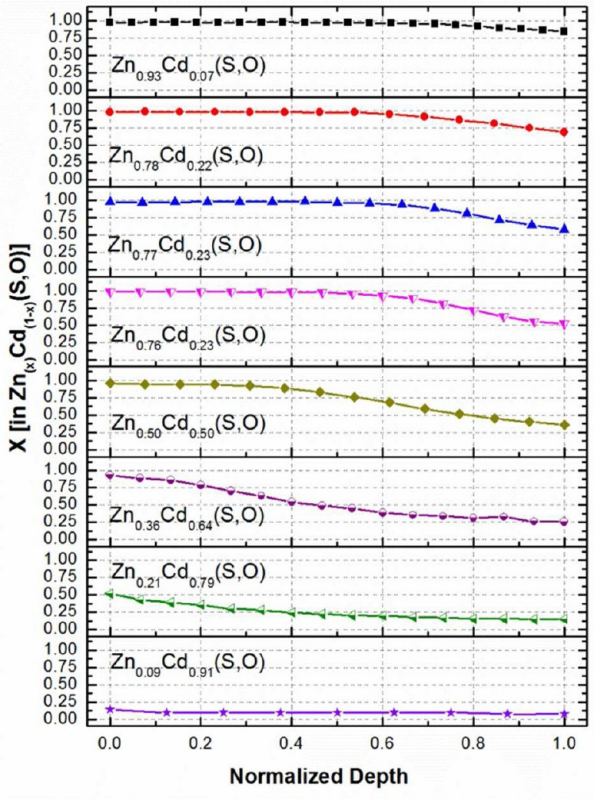

Figure 9. Film composition x as a function of dimensionless position in $Zn_xCd_{1-x}(S,O)$ films.

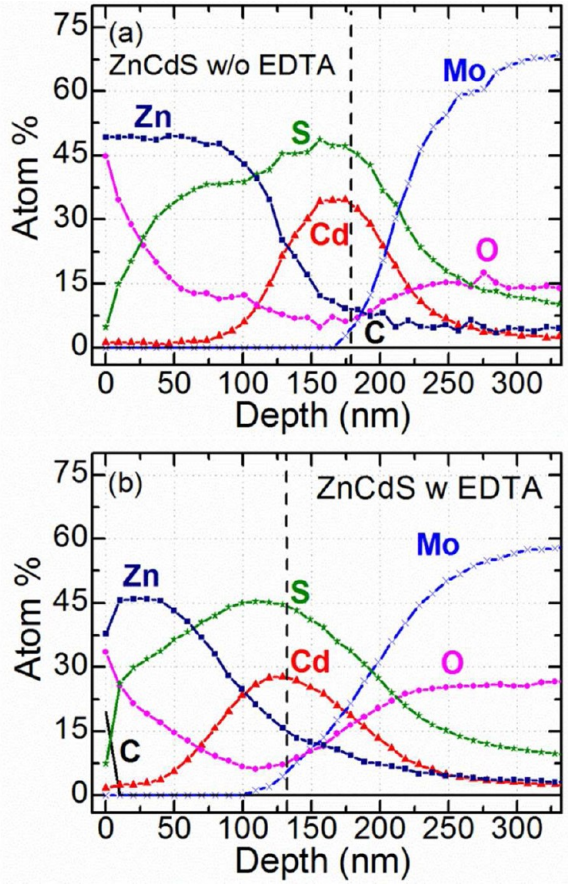

Figure 10. Auger depth profiles for films deposited (a) without and (b) with 0.02 M EDTA added to the chamical bath. Ammonium hydroxide, thiourea, $ZnSO_4$, and $CdSO_4$ concentrations were 3 M, 0.6 M 39 mM, and 1.33 mM, respectively.

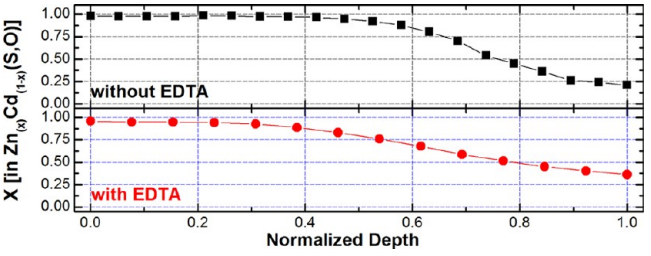

Figure 11. Film composition x as a function of dimensionless position in films deposited with and without EDTA. The films and the deposition conditions are same as those in Figure 10.

sulfur are detected well into the Mo film indicating significant diffusion, most likely due to diffusion along the Mo grain boundaries.

Figure 7a shows the elemental Auger depth profile of a 204 nm thick ZnS film. Figure 7b and 7c shows selected Auger electron spectra recorded as one approaches and sputters through the Mo−ZnS film interface. The ZnS film shows 15% oxygen incorporation in the film.

Figure 8 shows the Auger depth profile for $Zn_xCd_{1-x}(S,O)$ films where the spatially averaged x is varied by changing the initial $ZnSO_4$ and $CdSO_4$ concentrations (Table 1). Figure 9 shows the corresponding variation of x as a function of depth. All depth profiles show that the film composition is not homogeneous and x varies along the film thickness. The underlying reason behind the concentration gradients is the different reactivities of Cd^{2+} and Zn^{2+} and the differences in the solubility products of CdS and ZnS. The solubility product of CdS is smaller than ZnS, which leads to faster nucleation and growth of CdS as compared to ZnS.[42] For example; Figure 8a shows the Auger depth profile for the $Zn_{0.93}Cd_{0.07}S$ film. The Cd concentration in the film is highest near the Mo−$Zn_{0.93}Cd_{0.07}S$ interface and decreases slowly towards the film's surface. It appears that this film is cubic ZnS with Cd incorporated into this cubic lattice to form an alloy. Although the thickness-averaged Cd concentration is 7 %, it decreases monotonically from approximately 18 % near the Mo surface to nearly zero at the film surface. This decrease is due to rapid depletion of Cd through homogeneous nucleation and growth. Similar Cd concentration depth profiles are observed in films where the average x is low. For example, Figure 8b shows the Auger depth profile for the $Zn_{0.78}Cd_{0.22}S$ film. The Cd concentration decreases monotonically from 38 % near the Mo surface to nearly zero within 70 nm of the interface. The thickness-averaged Cd concentration in this film is approximately 22 % even though the top 80 nm of the film is entirely ZnS. Interestingly, a wide range of $ZnSO_4$-to-$CdSO_4$ ratios (40−200, Figure 4) give films with nearly the same overall composition (Table 1 and Figures 8b−8d) but with different film thicknesses.

Figure 8e shows the Auger depth profile for a film that has equal amounts of Zn and Cd concentrations ($Zn_{0.5}Cd_{0.5}S$). Figure 9 shows that the first 30 nm of this film near the Mo−$Zn_{0.5}Cd_{0.5}S$ interface is Cd-rich (x = 0.33, ~33 % Zn and ~67 % Cd). Towards the surface the Zn concentration rises, while Cd concentration decreases such that the top layers of the film are nearly all ZnS with very little Cd. The O and S

dx.doi.org/10.1021/am300771k | ACS Appl. Mater. Interfaces 2012, 4, 3676−3684

concentrations show the opposite trends in the top 100 nm of the film. The O concentration in the film follows that of Zn, rising with increasing Zn concentration while the S concentration decreases. This is consistent with the fact that $Zn(OH)_2$ reacts slower with S^{2-} than $Cd(OH)_2$ which leads to higher O concentration in regions of the film that grow after Cd has been depleted.

Figure 8f, 8g, and 8h shows the Auger depth profiles from films with average composition of x = 0.36, 0.21, and 0.09, respectively. In these cases, there is enough Cd in the CBD solution such that Cd is not depleted significantly during the growth and the entire film is $Zn_xCd_{1-x}(S,O)$. For x = 0.36 and x = 0.21, Zn is incorporated into the film nonuniformly and the Zn concentration rises monotonically from the Mo surface towards the film surface. For the film with x = 0.09, the Zn incorporation and film composition appears uniform on the scale of Figure 9 though there is a slow linear increase towards the surface.

When the initial CBD solution contains both $CdSO_4$ and $ZnSO_4$, we always observe a Cd-rich film near the interface with Mo. This is the desired concentration profile for buffer layers to be used with low band gap CIGS films because the conduction band offset is minimized. Moreover, increasing the Zn concentration towards the film surface would increase the light transmission by widening the band gap of the film towards the surface of the film.

Effect of EDTA on the Composition Depth Profile. Finally, we discuss the effects of EDTA on the Cd- and Zn-concentration depth profiles. All the films discussed so far have been deposited with EDTA added to the deposition solution. Addition of EDTA into the chemical bath slows down the deposition rate and results in more gradual changes in the Zn and Cd concentrations as a function of depth in the film than when EDTA is not used. Figure 10 compares the Auger depth profiles of the films deposited with and without EDTA. When EDTA is used, more Zn is incorporated into the film during the initial stages of the deposition and Zn concentration gradient becomes more gradual. This is most obvious from Figure 11, which shows variation of zinc fraction, x, as a function of depth. Cd-rich and Zn-rich layers appear more segregated when EDTA is not used. Addition of EDTA also appears to decrease O incorporation most likely due to EDTA chelation of Zn. Zn chelation decreases the zinc ion concentration and slows down the zinc hydroxide formation in the solution. This, in turn, decreases the oxygen concentration in the film.

CONCLUSIONS

The structure and chemical composition of $Zn_xCd_{1-x}(S,O)$ films deposited using the CBD method were studied in detail. ZnS and CdS films are primarily cubic and hexagonal, respectively. These are the predicted thermodynamically stable phases for ZnS and CdS. The Zn-rich films (e.g., x > 0.5) are primarily cubic ZnS with Cd incorporated into the film. For these films, the Cd concentration decreases from the film–substrate interface towards the film's surface. In fact, depending on the deposition time, Cd in the bath can be depleted completely such that the top portion of the film is ZnS. This Cd-rich region near the interface is attributed to faster reaction of Cd compared to Zn. The composition gradients that yield Cd-rich region near the substrate surface are favorable for solar cells based on low band gap CIGS films.

AUTHOR INFORMATION

Corresponding Author

*E-mail: aydil@umn.edu.

Notes

The authors declare no competing financial interest.

ACKNOWLEDGMENTS

The authors acknowledge funding from the Department of Energy. Initial studies on ZnS films were funded by a grant from the University of Minnesota's Institute for Renewable Energy and the Environment and extended to ZnCdS alloys by a Sunshot grant from the Department of Energy (#DE-EE0005319).

REFERENCES

(1) Jackson, P.; Hariskos, D.; Lotter, E.; Paetel, S.; Wuerz, R.; Menner, R.; Wischmann, W.; Powalla, M. *Prog. Photovoltaics* **2011**, *19*, 894.
(2) Baer, M.; Repins, I.; Contreras, M. A.; Weinhardt, L.; Noufi, R.; Heske, C. *Appl. Phys. Lett.* **2009**, *95*, 052106.
(3) Repins, I.; Contreras, M. A.; Egaas, B.; DeHart, C.; Scharf, J.; Perkins, C. L.; To, B.; Noufi, R. *Prog. Photovoltaics* **2008**, *16*, 235.
(4) Jager-Waldau, A. *Sol. Energy Mater. Sol. Cells* **2011**, *95*, 1509.
(5) Green, M. A.; Emery, K.; Hishikawa, Y.; Warta, W. *Prog. Photovoltaics* **2012**, *20*, 12.
(6) Wolden, C. A.; Kurtin, J.; Baxter, J. B.; Repins, I.; Shaheen, S. E.; Torvik, J. T.; Rockett, A. A.; Fthenakis, V. M.; Aydil, E. S. *J. Vac. Sci. Technol. A* **2011**, *29*, 030801.
(7) O'Brien, P.; McAleese, J. *J. Mater. Chem.* **1998**, *8*, 2309.
(8) Mokili, B.; Charreire, Y.; Cortes, R.; Lincot, D. *Thin Solid Films* **1996**, *288*, 21.
(9) Nakada, T.; Mizutani, M. *Jpn. J. Appl. Phys.* **2002**, *41*, L165.
(10) Nakada, T.; Mizutani, M.; Hagiwara, Y.; Kunioka, A. *Sol. Energy Mater. Sol. Cells* **2001**, *67*, 255.
(11) Contreras, M. A.; Romero, M. J.; Hasoon, B. T. E.; Noufi, R.; Ward, S.; Ramanthan, K. *Thin Solid Films* **2002**, *403*, 204.
(12) Enriguez, J. P.; Mathew, X. *Sol. Energy Mater. Sol. Cells* **2003**, *76*, 313.
(13) Herrero, J.; Gutierrez, M. T.; Guillen, C.; Dona, J. M.; Martinez, M. A.; Chaparro, A. M.; Bayon, R. *Thin Solid Films* **2000**, *361*, 28.
(14) Siebentritt, S. *Sol. Energy* **2004**, *77*, 767.
(15) Dona, J. M.; Herrero, J. *J. Electrochem. Soc.* **1997**, *144*, 4081.
(16) Ruffner, J. A.; Himel, M. D.; Mizrahi, V.; Stegeman, G. I.; Gibson, U. *Appl. Opt.* **1989**, *28*, 5209.
(17) Abounadi, A.; Diblasio, M.; Bouchara, D. *Phys. Rev. B* **1994**, *50*, 11677.
(18) Chamberlin, R. R.; Skarman, J. S. *J. Electrochem. Soc.* **1966**, *113*, 86.
(19) Xian, H.; Benalloul, P.; Barthou, C.; Benoit, J. *Thin Solid Films* **1994**, *248*, 193.
(20) Goto, F.; Ichimura, M.; Arai, E. *Jpn. J. Appl. Phys.* **1997**, *36*, L1146.
(21) Kavanagh, Y.; Alam, M. J.; Cameron, D. C. *Thin Solid Films* **2004**, *447*, 85.
(22) Bakke, J. R.; Jung, H. J.; Tanskanen, J. T.; Sinclair, R.; Bent, S. F. *Chem. Mater.* **2010**, *22*, 4669.
(23) Nakada, T. *Thin Solid Films* **2000**, *361*, 346.
(24) Chu, T. L.; Chu, S. S.; Britt, J.; Ferekides, C.; Wu, C. Q. *J. Appl. Phys.* **1991**, *70*, 2688.
(25) Mitzi, D. B.; Gunawan, O.; Todorov, T. K.; Wang, K.; Guha, S. *Solar Energy Mater. Sol. Cells* **2011**, *95*, 1421.
(26) Burton, L. C.; Hench, T. L. *Appl. Phys. Lett.* **1976**, *29*, 612.
(27) Yamaguchi, T.; Yamamoto, Y.; Tanaka, T.; Yoshida, A. *Thin Solid Films* **1999**, *343*, 516.
(28) Nakada, T.; Furumi, K.; Kunioka, A. *IEEE Trans. Electron. Dev* **1999**, *46*, 2093.
(29) Nakada, T.; Mizutani, M. *Jpn. J. Appl. Phys. 2* **2002**, *41*, L165.

(30) Nakada, T.; Hongo, M.; Hayashi, E. *Thin Solid Films* **2003**, *431*, 242.
(31) Sartale, S. D.; Sankapal, B. R.; Lux-Steiner, M.; Ennaoui, A. *Thin Solid Films* **2005**, *480*, 168.
(32) Bhattacharya, R. N.; Contreras, M. A.; Teeter, G. *Jpn. J. Appl. Phys. 2* **2004**, *43*, L1475.
(33) Ennaoui, A.; Bar, M.; Klaer, J.; Kropp, T.; Saez-Araoz, R.; Lux-Steiner, M. C. *Prog. Photovoltaics* **2006**, *14*, 499.
(34) Bhattacharya, R. N.; Ramanathan, K. *Sol. Energy* **2004**, *77*, 679.
(35) Kundu, S.; Olsen, L. C. *Thin Solid Films* **2005**, *471*, 298.
(36) Yagioka, T.; Nakada, T. *Appl. Phys. Express* **2009**, *2*, 072201.
(37) Dona, J. M.; Herrero, J. *Thin Solid Films* **1995**, *268*, 5.
(38) Pudov, A.; Sites, J.; Nakada, T. *Jpn. J. Appl. Phys. 2* **2002**, *41*, L672.
(39) Bhattacharya, R. N.; Contreras, M. A.; Egaas, B.; Noufi, R. N.; Kanevce, A.; Sites, J. R. *Appl. Phys. Lett.* **2006**, *89*, 253503.
(40) Tanaka, K.; Minemoto, T.; Takakura, H. *Sol. Energy* **2009**, *83*, 477.
(41) Herz, K.; Eicke, A.; Kessler, F.; Wachter, R.; Powalla, M. *Thin Solid Films* **2003**, *431*, 392.
(42) Li, Z. Q.; Shi, J. H.; Liu, Q. Q.; Wang, Z. A.; Sun, Z.; Huang, S. M. *Appl. Surf. Sci.* **2010**, *257*, 122.
(43) Vallejo, W.; Hurtado, M.; Gordillo, G. *Electrochim. Acta* **2010**, *55*, 5610.
(44) Islam, M. M.; Ishizuka, S.; Yamada, A.; Sakurai, K.; Niki, S.; Sakurai, T.; Akimoto, K. *Solar Energy Mater. Sol. Cells* **2009**, *93*, 970.
(45) Gal, D.; Hodes, G.; Hariskos, D.; Braunger, D.; Schock, H.-W. *Appl. Phys. Lett.* **1998**, *73*, 3135.
(46) Song, J.; Li, S. S.; Chen, L.; Noufi, R.; Anderson, T. J.; Crisalle, O. D. *Conf. Rec. IEEE Photovoltaic Spec. Conf., 4th* **2006**, *1*, 534.
(47) Gloeckler, M.; Sites, R. S. *Thin Solid Films* **2005**, *480-481*, 241.
(48) Padam, G. K.; Malhotra, G. L.; Rao., S. U. M. *J. Appl. Phys.* **1988**, *63*, 770.
(49) Zhang, Y.; Dang, X. Y.; Jin, J.; Yu, T.; Li, B. Z.; He, Q.; Li, F. Y.; Sun, Y. *Appl. Surf. Sci.* **2010**, *256*, 6871.
(50) Dona, J. M.; Herrero, J. *J. Electrochem. Soc.* **1994**, *141*, 205.
(51) Kaur, I.; Pandya, D. K.; Chopra, K. L. *J. Electrochem. Soc.* **1980**, *127*, 943.
(52) Naghavi, N.; Hubert, C.; Etcheberry, A.; Bermudez, V.; Hariskos, D.; Powalla, M.; Linot, D. *Prog. Photovoltaics* **2009**, *17*, 1.
(53) Hodes, G. *Chemical Solution Deposition of Semiconductor Films*; Marker Dekker Inc.: New York, NY, 2003.
(54) Wright, K.; Gale, J. D. *Phys. Rev. B* **2004**, *70*, 035211.